


Optical and excitonic properties of transition metal oxide perovskites by the Bethe-Salpeter equation

Lorenzo Varrassi,¹ Peitao Liu ,² Zeynep Ergönenc Yavas,³ Menno Bokdam,⁴ Georg Kresse ,² and Cesare Franchini ^{1,2}¹*Dipartimento di Fisica e Astronomia, Università di Bologna, 40127 Bologna, Italy*²*University of Vienna, Faculty of Physics and Center for Computational Materials Science, Kolingasse 14-16, A-1090 Vienna, Austria*³*Turkish Aerospace Industries, Inc., Department of Materials Engineering, Fethiye Mahallesi, Havacılık Bulvarı Number 17, 06980 Kazan-Ankara, Turkey*⁴*University of Twente, Faculty of Science and Technology and MESA + Institute, Enschede, Netherlands*

(Received 2 May 2021; accepted 23 June 2021; published 9 July 2021)

We present a systematic investigation of the role and importance of excitonic effects on the optical properties of transition metal oxide perovskites. A representative set of 14 compounds has been selected, including 3d (SrTiO₃, LaScO₃, LaTiO₃, LaVO₃, LaCrO₃, LaMnO₃, LaFeO₃, and SrMnO₃), 4d (SrZrO₃, SrTcO₃, and Ca₂RuO₄) and 5d (SrHfO₃, KTaO₃, and NaOsO₃) perovskites, covering a band gap ranging from 0.1 eV to 6.1 eV and exhibiting different electronic, structural, and magnetic properties. Optical conductivities and optical transitions including electron-hole interactions are calculated through the solution of the Bethe-Salpeter equation (BSE) with quasiparticle energies evaluated by the single-shot G_0W_0 approximation. The exciton binding energies are computed by means of a model BSE, carefully benchmarked against the full-BSE method, in order to obtain well-converged results in terms of k -point sampling. The predicted results are compared with available measured data, with an overall satisfactory agreement between theory and experiment.

DOI: [10.1103/PhysRevMaterials.5.074601](https://doi.org/10.1103/PhysRevMaterials.5.074601)

I. INTRODUCTION

The study of transition metal oxide (TMO) perovskites has brought to light a wide array of physical and chemical properties, including colossal magnetoresistance [1,2], multiferroicity [3], metal-insulator transitions [4], superconductivity [5,6], two-dimensional electron gas [7], and spin and charge ordering [8]. In the last decades the 4d and 5d TMO perovskites have gained increasing interest due to the discovery of novel electronic and magnetic quantum states of matter arising from the coupling between spin-orbit interaction and other active degrees of freedom [9–12]. Up to now, few theoretical studies have investigated the role of excitonic effects on the optical spectra of TMO perovskites [13–17]. These works have proved that the random phase approximation (RPA) is able to reproduce the experimental data only to a limited extent and that the inclusion of electron-hole (e-h) interaction is often pivotal to achieve a satisfying account of the optical transitions [14–16]. This paper attempts to extend the study of excitonic effects from individual compounds toward a larger representative data set, aiming to contribute to a comprehensive understanding of the role the electron-hole interaction in TMO perovskites.

In order to compute the optical properties, we solve the Bethe-Salpeter equation (BSE) [18,19] through a direct diagonalization scheme, which offers direct access to excitonic wave functions and allows for a more transparent interpretation of the main features of the optical spectra. To correctly estimate the interband optical transition energies it is necessary to accurately calculate the quasiparticle energies and, above all, the fundamental gaps. Density functional theory

(DFT) is usually considered not suitable in this regard; it commonly underestimates fundamental gaps and does not provide a reliable account of the excited state properties [20]. This task is instead successfully achieved by the GW approximation [21–23], which provides a good description of insulating gaps and band dispersions for the TMO perovskites [24–28]. To accurately predict optical properties it is therefore natural to combine GW and BSE in a single computational protocol. However, the resulting $GW+BSE$ procedure is computationally very demanding. On the one hand, both GW and BSE are notoriously computationally expensive, with an unfavorable scaling (both standard implementations exhibit at least quartic scaling in the system size and quadratic in the number of k points [29]); their application to large systems therefore presents a technical challenge. On the other hand, to obtain reliable results, a precise convergence procedure is needed as pointed out in seminal BSE studies [19,30]. For example, a too sparse k -point mesh may introduce spurious artifacts [31,32] or incorrect estimations of the exciton binding energy [33,34]. To bypass these limitations alternative schemes have been proposed, from shifted [29,35] or hybrid k -point meshes [33] to interpolation schemes [36] or methods based on density matrix perturbation theory [37]. Additional complications arise from the fact that the considered materials cover a wide range of electronic and excitonic behaviors, with gaps ranging from 0.1 eV to 6.0 eV and originating from different mechanisms (band insulator, Mott-Hubbard, Mott-Dirac, etc.). This unavoidably affects the nature and properties of the exciton wave functions. These fundamental characteristics have in turn a strong impact on the convergence rate of optical properties [31], especially with respect to the k -point sampling of the

TABLE I. Material data set and main computational parameters. The first column lists the considered compounds. The second set of columns collects information on the crystal structures (C = cubic, O = orthorhombic, M = monoclinic), electronic configurations of the transition metal d shell, and ground state magnetic orderings (NM = nonmagnetic and different types of antiferromagnetic spin configurations [38]). The last set of columns lists the relevant computational parameters: plane-wave energy cutoff for orbitals (E_{pw}), number of bands (N_{pw}), number of frequency points used for the calculation of the GW polarizability (N_{ω}). N_O and N_C refer to the number of occupied and conduction bands, respectively, included in the BSE equation. The plane-wave energy cutoff for the response function is chosen to be $(2/3)E_{pw}$.

	Crystal Structures	Electronic Configurations	Magnetic Orderings	E_{pw} (eV)	N_{pw}	N_{ω}	N_O	N_C
SrTiO ₃	C- $P_{m\bar{3}m}$	$3d^0$	NM	600	512	96	12	10
SrZrO ₃	C- $P_{m\bar{3}m}$	$4d^0$	NM	650	1972	64	12	12
SrHfO ₃	C- $P_{m\bar{3}m}$	$5d^0$	NM	650	2304	96	12	13
KTaO ₃	C- $P_{m\bar{3}m}$	$5d^0$	NM	500	896	96	12	12
LaScO ₃	O- P_{nma}	$3d^0$	NM	500	1280	64	32	32
LaTiO ₃	O- P_{nma}	$3t_{2g}^1$	G-AFM	500	448	64	34	34
LaVO ₃	M- $P_{21/b}$	$3t_{2g}^2$	G-AFM	500	448	64	30	30
LaCrO ₃	O- P_{nma}	$3t_{2g}^3$	G-AFM	500	448	64	32	32
LaMnO ₃	O- P_{nma}	$3t_{2g}^3 e_g^1$	A-AFM	500	448	64	26	26
LaFeO ₃	O- P_{nma}	$3t_{2g}^3 e_g^2$	G-AFM	500	448	96	34	34
SrMnO ₃	C- $P_{m\bar{3}m}$	$3t_{2g}^3$	G-AFM	500	448	64	29	29
SrTcO ₃	O- P_{nma}	$4t_{2g}^3$	G-AFM	500	512	64	30	30
Ca ₂ RuO ₄	O- P_{nma}	$4t_{2g}^3 e_g^1$	AFM	500	512	64	30	37
NaOsO ₃	O- P_{bca}	$5t_{2g}^3$	G-AFM	500	448	64	30	30

Brillouin zone (BZ). Therefore, in order to achieve converged and reliable exciton binding energies and ensure equally well-defined results for all compounds in the data set, we adopted a model-BSE (mBSE) procedure, which uses a parametrized model for the dielectric screening [15,34].

Following the work of He *et al.* [38] and Ergörenc *et al.* [24], we adopt a representative data set of 14 TM perovskites that includes compounds with different electronic, structural, magnetic, and dielectric properties, as summarized in Table I and in Refs. [24]: specifically, (i) insulating gaps ranging from 0.1 eV to 6 eV; (ii) $3d$, $4d$, and $5d$ TM-based perovskites with different orbital occupancy; (iii) nonmagnetic and differently ordered AFM patterns; (iv) various crystal structures with different types of internal structural distortions (e.g., with and without Jahn-Teller instabilities); (v) macroscopic dielectric constant from 1 to 10. The complete atomic positions, as well as the experimental sources, are given in the Supplemental Material (SM) [39]. We note that in order to correctly describe the G-AFM magnetic ordering a supercell containing four formula units was used.

The paper is organized as follows: Section II describes the computational setup, with a particular focus on the k -point convergence procedure. The discussion of the optical properties is divided into three sections, each for a specific subgroup of materials: Sec. III A for the C- $P_{m\bar{3}m}$ perovskites, Sec. III B for the La TMO_3 series, and Sec. III C for Ca₂RuO₄, NaOsO₃, SrMnO₃, and SrTcO₃, followed by the conclusion in Sec. IV.

II. COMPUTATIONAL DETAILS

All *ab initio* calculations were performed using the Vienna *ab initio* Simulation Package (VASP) [40,41] with the

augmented wave method (PAW) [42]. The potential types are listed in Table II; the GW versions of all PAW potentials were used. The ultrasoft (US) versions of the potentials were used for all materials except for Sr and Ti in SrTiO₃, for which the norm-conserving (NC) versions were used, consistently with Ergörenc *et al.* [24]. The procedure used to determine the optical conductivity for each material involves three main steps:

(1) The first one is a standard self-consistent DFT calculation using the generalized gradient approximation (GGA) parametrized by Perdew, Burke, and Ernzerhof (PBE) [43]. For LaTiO₃ and LaVO₃ PBE alone is not able to open the gap; therefore a small effective on-site Hubbard $U_{\text{eff}} = 2$ eV [24] was added, using the DFT+ U formulation of Dudarev [44]. The spin-orbit coupling (SOC) is included for NaOsO₃ [45].

(2) The second step consists of a single-shot G_0W_0 variant of the GW approximation: in the employed implementation [46] the one-particle Green's functions are constructed from the previously determined PBE one-electron energies and orbitals, while the dynamically screened Coulomb interaction W is computed within the framework of the RPA [46,47]. The convergence of the quasiparticle (QP) energies for this data set has been previously investigated by Ergörenc *et al.* [24]. The energy cutoffs, number of bands, and numbers of frequency points, summarized in Table I, are chosen consistently with the setup adopted in Ref. [24] in order to ensure converged QP gaps within an accuracy of approximately 100 meV. The choice of the k -point mesh has a paramount impact on the convergence of the optical properties, which will be discussed in detail in Sec. II A.

(3) The optical conductivities, both in the RPA [48] and in the BSE [19,49,50], are calculated from the G_0W_0 data. The Tamm-Dancoff approximation (TDA) [51] is used;

TABLE II. List of radial cutoff parameters (core radii, in atomic units) for each angular quantum number and default E_{pw} in eV for all potentials employed. The *GW* ultrasoft (GW-US) versions of the PAW potentials were used for all materials except for SrTiO₃, which employed the norm-conserving *GW* (GW-NC) ones.

Element	PAW	r_s	r_p	r_d	r_f	E_{pw}
O	GW-US	1.2	1.5	1.6	1.4	434
	GW-NC	1.0	1.1	1.1		765
Na	GW-US	1.6	2.0	2.2		260
K	GW-US	1.7	2.0	2.5		249
Ca	GW-US	1.6	1.9	2.2		281
Sc	GW-US	1.7	1.7	1.9	2.0	379
Ti	GW-US	1.7	1.7	2.0	2.0	384
	GW-NC	0.9	1.4	1.9		785
V	GW-US	1.8	1.7	1.9	2.0	382
Cr	GW-US	2.8	2.5	2.5	2.8	219
Mn	GW-US	1.6	1.7	1.9	1.9	385
Fe	GW-US	1.5	1.7	1.9	2.0	388
Sr	GW-US	1.7	2.1	2.5	2.5	225
	GW-NC	1.1	2.0	2.3		543
Zr	GW-US	1.3	1.8	2.0	2.1	346
Tc	GW-US	1.5	1.8	2.2	2.3	318
Ru	GW-US	1.5	1.8	2.2	2.3	321
La	GW-US	1.6	1.8	2.2	2.5	314
Hf	GW-US	1.5	1.9	2.2	2.5	283
Ta	GW-US	1.5	1.9	2.2	2.5	286
Os	GW-US	1.5	1.8	2.2	2.3	319

this approximation has been proven to be reliable for the prediction of optical spectra for standard semiconductors [50].

The frequency-dependent macroscopic dielectric function is calculated as [15,50]

$$\varepsilon(\omega) = 1 - \lim_{\mathbf{q} \rightarrow 0} V(\mathbf{q}) \sum_{\Lambda} \left(\frac{1}{\omega - E^{\Lambda} + i\eta} - \frac{1}{\omega + E^{\Lambda} - i\eta} \right) \times \left\{ \sum_{\mathbf{k}} w_{\mathbf{k}} \sum_{v,c} \langle \psi_{c\mathbf{k}} | e^{i\mathbf{q}\cdot\mathbf{r}} | \psi_{v\mathbf{k}} \rangle A_{cv\mathbf{k}}^{\Lambda} \right\} \times \{\text{c.c.}\}, \quad (1)$$

where E^{Λ} and $A_{cv\mathbf{k}}^{\Lambda}$ are the BSE eigenvalues and eigenvectors, V is the bare Coulomb interaction, $w_{\mathbf{k}}$ are the k -point weights, η a positive infinitesimal, and $\psi_{c\mathbf{k}}$ and $\psi_{v\mathbf{k}}$ are respectively the unoccupied and occupied DFT wave functions. The oscillator strengths S_{Λ} associated with the optical transitions are defined as [15]

$$S_{\Lambda} = \text{Tr} \left[\sum_{\mathbf{k}} w_{\mathbf{k}} \sum_{v,c} \langle \psi_{c\mathbf{k}} | e^{i\mathbf{q}\cdot\mathbf{r}} | \psi_{v\mathbf{k}} \rangle A_{cv\mathbf{k}}^{\Lambda} \times \{\text{c.c.}\} \right]. \quad (2)$$

The exciton binding energies E_{xb} are computed as the difference between the first bright BSE transition and the fundamental G_0W_0 gap. The optical results will be interpreted in Sec. III A 2 in terms of the joint density of states (JDOS) defined as

$$\text{JDOS}(\omega) = 2 \sum_{v,c,\mathbf{k}} w_{\mathbf{k}} \delta(E_c(\mathbf{k}) - E_v(\mathbf{k}) - \hbar\omega),$$

where $E_c(\mathbf{k})$ and $E_v(\mathbf{k})$ are the G_0W_0 eigenvalues; the Dirac δ is approximated by a normalized Gaussian function with a broadening parameter of 0.10 eV.

A. k -point convergence

It is well known that optical properties exhibit a strong dependence on k -point sampling and generally very dense k -point meshes are required to obtain well-converged optical conductivities [30,33,35,52,53]. It should be noted that in cases where the exciton is spatially highly delocalized it is more efficient to use dense meshes only in a small portion of the Brillouin zone (around Γ), rather than sampling the full k space, as recently discussed by Umari in Ref. [53]. In this work, to obtain reliable results we carried out a careful k -point convergence procedure; the convergence criteria employed are based on the accurate quantification of the first BSE eigenvalue E^{Λ} related to a nondark exciton within an accuracy of 5 meV. Considering the huge computational cost that a *GW*+BSE calculation on a dense k -point grids may involve, results on dense converged k meshes as well as the convergence tests themselves cannot be efficiently done at the standard *GW*+BSE level. To mitigate these limitations, two different strategies were adopted: (i) mBSE and (ii) k -averaging. The mBSE scheme is used to perform the convergence tests and to determine the E_{xb} values, while the k -averaging technique is employed to calculate the optical conductivity spectra $\sigma(\omega)$.

1. Model BSE

The mBSE approach [33,34] introduces two approximations to the standard BSE scheme:

(1) Model dielectric screening approximation: The RPA dielectric function calculated in the G_0W_0 step is

TABLE III. Converged k -point grids, volumes of the Brillouin zone, and k -point densities for the listed materials. The k -point density is calculated as the total number of k points divided by the Brillouin zone volume. A k -point mesh is considered converged when the BSE eigenvalue related to the first nondark eigenvector is determined within an accuracy of 5 meV.

	Converged k mesh	Brillouin zone volume (\AA^{-3})	k -point density (kpts/ \AA^{-3})
SrTiO ₃	$20 \times 20 \times 20$	4.17	1920
SrZrO ₃	$20 \times 20 \times 20$	3.57	2240
SrHfO ₃	$20 \times 20 \times 20$	3.56	2240
KTaO ₃	$20 \times 20 \times 20$	3.91	2040
LaScO ₃	$10 \times 10 \times 6$	0.93	640
LaTiO ₃	$10 \times 10 \times 6$	1.00	600
LaVO ₃	$10 \times 10 \times 6$	1.03	580
LaCrO ₃	$10 \times 10 \times 6$	1.06	570
LaMnO ₃	$10 \times 10 \times 6$	1.02	590
LaFeO ₃	$10 \times 10 \times 6$	1.02	590
SrMnO ₃	$8 \times 8 \times 4$	1.11	230
SrTcO ₃	$9 \times 9 \times 6$	1.02	480
Ca ₂ RuO ₄	$8 \times 8 \times 4$	0.70	370
NaOsO ₃	$9 \times 9 \times 6$	1.14	430

approximated by an analytic model [34]

$$\epsilon_{\mathbf{G},\mathbf{G}}^{-1}(\mathbf{k}) = 1 - (1 - \epsilon_{\infty}^{-1}) \exp\left[-\frac{|\mathbf{k} + \mathbf{G}|^2}{4\lambda^2}\right], \quad (3)$$

where ϵ_{∞} is the static ion-clamped dielectric function and λ the range separation parameter, which is determined by fitting $\epsilon_{\mathbf{G},\mathbf{G}}^{-1}(\mathbf{k})$ to the RPA-calculated one. The off-diagonal elements of the inverse dielectric function are neglected rendering the screened Coulomb kernel diagonal ($\mathbf{G} = \mathbf{G}'$). This analytical model has proven to be a good approximation to the full dielectric function [54].

(2) The QP energies are approximated through the application of a scissor operator to the DFT one-electron energies (such that the resulting band gap matches the G_0W_0 one).

This approach reduces the overall computational cost and was successfully applied to halide perovskites [34,55], iridates [15], and 3d TMOs [56], and it has been shown to correctly reproduce the full-BSE spectrum up to 6 eV for SrTiO₃ [16]. All scissor operators used, along with λ and ϵ_{∞}^{-1} , are detailed in the Supplemental Material [39]. The k -point grids that ensure the required E_{xb} accuracy are presented in Table III and range from $8 \times 8 \times 4$ to $20 \times 20 \times 20$, depending on the system. We note that the cubic ($C-P_{m\bar{3}m}$) perovskites require considerably denser k meshes than the magnetic compounds. Nevertheless, even a $20 \times 20 \times 20$ mesh does not yield a fully converged $\sigma(\omega)$ over the entire energy range (see for example SrTiO₃ and KTaO₃ in Fig. 1). This is due to the large spatial delocalization of the excitonic wave function in these materials, as discussed below. In contrast, for all remaining perovskites a fully converged $\sigma(\omega)$ has been obtained, and even sparser k -point meshes are able to reproduce the spectra (see Fig. 1). This behavior can be traced back to the different degree of localization of the first nondark BSE eigenvectors $A_{c\mathbf{k}}^{\Lambda}$, illustrated as contour plots of the squared modulus $\sum_{v,c} |A_{c\mathbf{k}}^{\Lambda}|^2$ in k space for selected examples in Fig. 2. The cubic compounds exhibit an excitonic wave function strongly localized around the Γ point in the BZ. This in turn imposes the necessity of very dense k -point meshes to correctly describe $A_{c\mathbf{k}}^{\Lambda}$ [31,57] and to avoid spurious artificial confinement

effects [58], which can be achieved by selectively increasing the k -point density around Γ (this could be achieved within a regular-grid procedure by setting to zero all contributions to the excitonic amplitude beyond a cutoff volume around Γ [53]). The remaining perovskites show excitonic wave functions that span a larger portion of the BZ and thus require a less dense BZ sampling.

2. k -averaging

A k -averaging procedure was adopted to calculate the full-BSE spectra [15,50]. This averaging procedure includes two steps: in the first step all L irreducible k points $\mathbf{k}_1, \dots, \mathbf{k}_L$ from a Γ -centered $n \times n \times n$ grid are generated; in the second step L independent $GW + BSE$ calculations are executed. Each calculation is based on an $m \times m \times m$ grid, shifted by the corresponding $\mathbf{k}_1, \dots, \mathbf{k}_L$. The final dielectric function is therefore attained by averaging over the previous results:

$$\epsilon(\omega) = \frac{1}{W} \sum_{p=1}^L w_{\tilde{\mathbf{k}}_p} \epsilon_{\tilde{\mathbf{k}}_p}(\omega), \quad W = \sum_{p=1}^L w_{\tilde{\mathbf{k}}_p}, \quad (4)$$

where $\epsilon_{\tilde{\mathbf{k}}}$ is the dielectric function calculated on the mesh shifted by $\tilde{\mathbf{k}}$. The final result, which includes all k points of a regular $(n \cdot m) \times (n \cdot m) \times (n \cdot m)$ calculation, is denoted by $m \times m \times m | n \times n \times n$. This k -averaging approach implicitly involves an approximation [50]: the long-range part of the Coulomb kernel is truncated at $\sim m$ times the unit cell size and consequently may cause spurious artifacts for extended real-space exciton wave functions. The cubic ($C-P_{m\bar{3}m}$) compounds, in particular, possess a (first nondark) exciton wave function strongly localized around Γ , which corresponds to a delocalized real-space wave function and requires therefore careful testing. The magnetic TMO perovskites are instead less affected by the risk of spurious artifacts due to a more delocalized exciton wave function in reciprocal space.

The employed n and m values were checked by comparing the averaged $\sigma(\omega)$ with a standard BSE calculation without k -averaging and investigating the presence of substantial peak enhancements and suppressions. The choice ($m = 4$, $n = 5$)

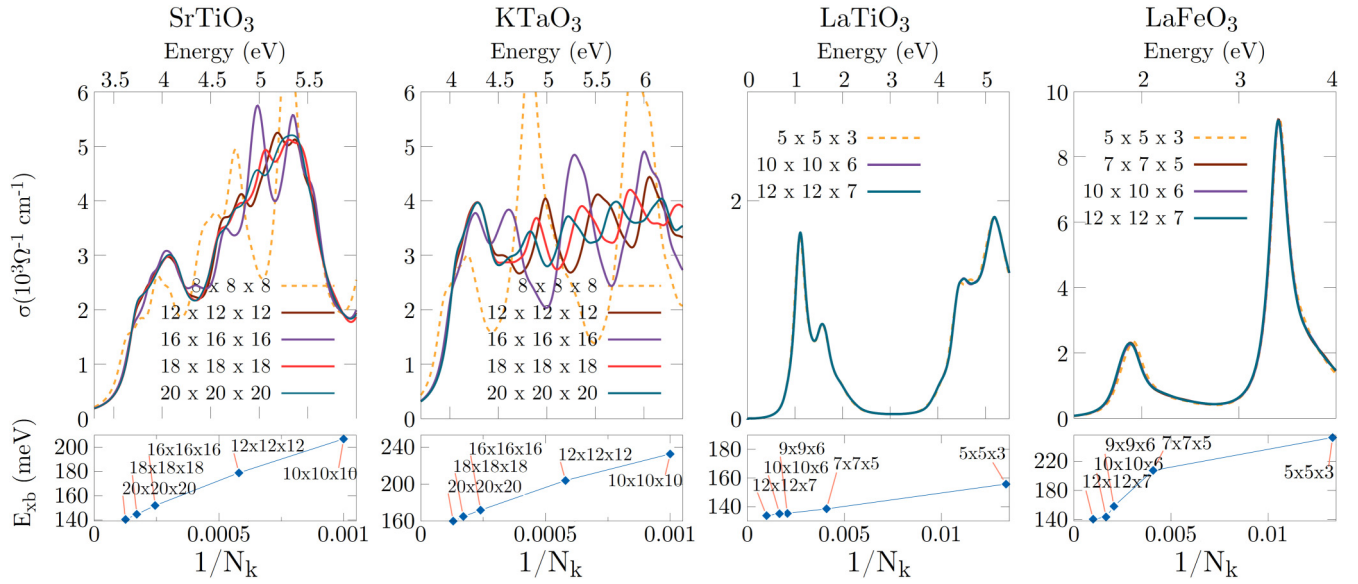


FIG. 1. Convergence tests for the mBSE-derived $\sigma(\omega)$ (top panels) and exciton binding energies E_{xb} (lower panels) with respect to the number of k points. The optical conductivities are expressed in $10^3 \Omega^{-1} \text{cm}^{-1}$.

does not introduce artificial artifacts in SrHfO₃, SrZrO₃, and KTaO₃; however to avoid a spurious peak suppression inside the SrTiO₃ optical spectrum, a larger $m = 7$ value is needed (see Supplement Material [39] for more details).

III. RESULTS AND DISCUSSION

The discussion of the results is divided into three sections, each focusing on a specific class of perovskites: (i) cubic nonmagnetic perovskites (SrTiO₃, SrZrO₃, SrHfO₃, and KTaO₃), (ii) the lanthanum series (LaScO₃, LaTiO₃, LaVO₃, LaCrO₃, LaMnO₃, and LaFeO₃), and (iii) Ca₂RuO₄, NaOsO₃, SrMnO₃, and SrTcO₃.

A. Cubic perovskites

1. Comparison between BSE and RPA spectra

The optical conductivity $\sigma(\omega)$ obtained through the k -averaging procedure for all cubic compounds is shown in Fig. 3. All spectra exhibit a similar line shape characterized by two main structures (designated by their most intense peaks p_1 and p_2) caused by the crystal field splitting of the TM- d states into t_{2g} and e_g subsets. We note that the very

sharp peak observed in SrTiO₃ at ≈ 6.4 eV has no analogs in the other cubic materials. Its origin has been examined by Refs. [14,16] and has been related to transitions to (low dispersing) localized Ti- e_g states along the Γ -X direction in the BZ. Sponza *et al.* [14] discussed the neglect of coupling terms (i.e., electron-phonon interaction or the dynamical screening) of the standard BSE approach as a possible reason behind the exceedingly strong intensity of the peak, which does not appear in the experimental data.

The BSE improves considerably upon RPA the quantitative agreement with the experimental data, in particular for what concerns the intensities and energy positions of the first structures. The differences between the experimental centers of mass (COMs) of the p_1 structures and the BSE COMs are strongly reduced, with a mean absolute error of 0.24 eV compared to 1.00 eV for the RPA curves (see Fig. 4). Small residual discrepancies between BSE and measured curves are visible at the onset, especially for SrHfO₃ and SrZrO₃. Significant contributions to these discrepancies originate from differences between the experimental and G_0W_0 predicted gaps [24], equal to 0.30 eV (SrTiO₃, SrZrO₃) and 0.40 eV (SrHfO₃). The BSE-induced redshift of the p_1 structures

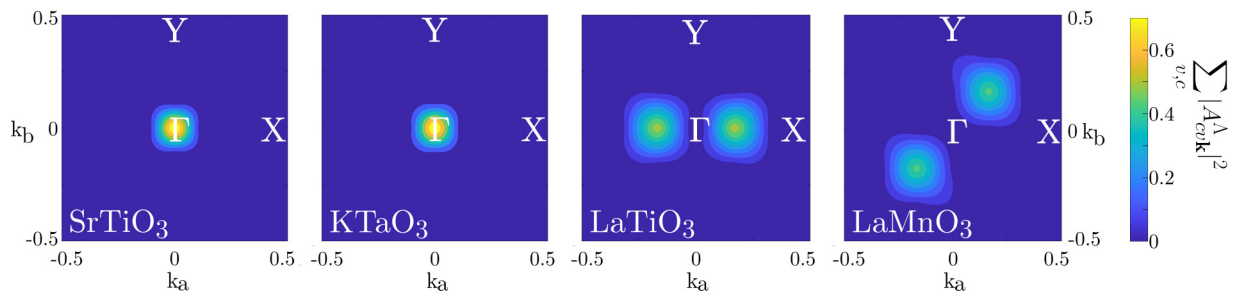


FIG. 2. Contour plots of the squared modulus $\sum_{v,c} |A_{cvk}^A|^2$ of the first nondark exciton for SrTiO₃, KTaO₃, LaTiO₃, and LaMnO₃ along the k_a - k_b plane ($k_c = 0$) in the Brillouin zone. The eigenvectors are calculated with the BSE scheme on a $8 \times 8 \times 8$ k mesh for SrTiO₃ and KTaO₃ and on a $6 \times 6 \times 4$ for LaTiO₃ and LaMnO₃.

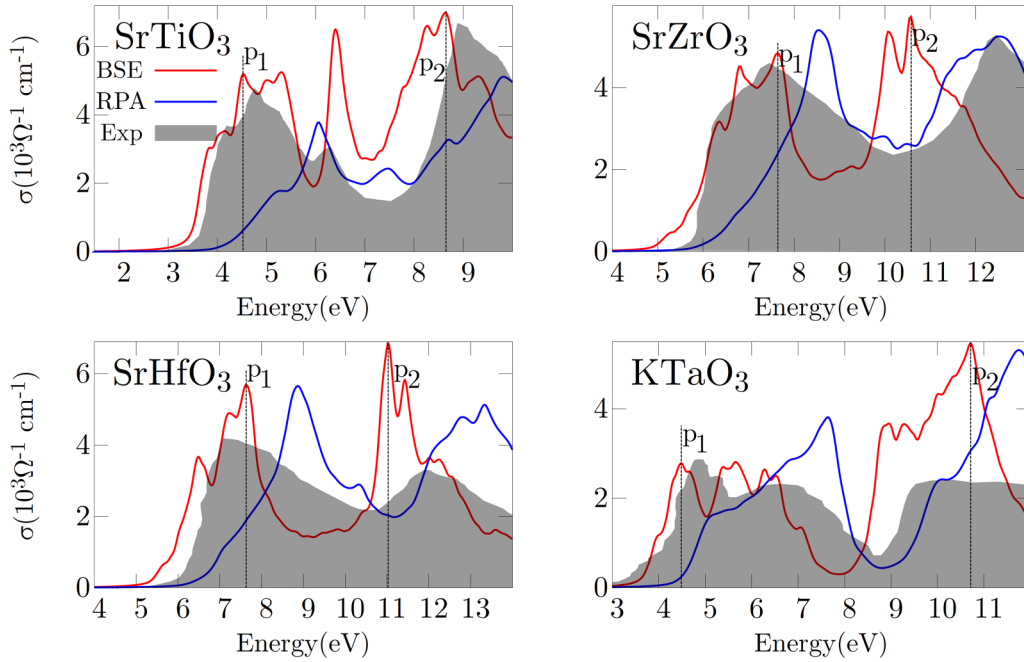


FIG. 3. Optical conductivity $\sigma(\omega)$ calculated within the RPA (blue line), BSE approach (red line), and experimental data. All curves are obtained through a $5 \times 5 \times 5 | 4 \times 4 \times 4$ k -averaging, except for SrTiO₃ which employed a $7 \times 7 \times 7 | 4 \times 4 \times 4$. The main two peaks of the BSE spectra of each structure are labeled as p_1 and p_2 .

[evaluated as the difference between the RPA and BSE spectra at the onset at $\sigma(\omega) \sim 1 \times 10^3 \Omega^{-1} \text{cm}^{-1}$] varies from 0.80 eV (KTaO₃) to 1.20 eV (SrTiO₃). Significant spectral weight transfers are thus visible, signaling strong excitonic contributions for the considered cubic systems.

The onsets for the p_2 structure are instead systematically underestimated by about 1–2 eV; for SrTiO₃ this deviation was attributed to excessively strong excitonic effects [14]. The mean absolute error between the BSE COMs of the p_2 structures and the experimental ones (see Fig. 4) is equal to –0.75 eV.

The exciton binding energies E_{xb} for different k meshes are listed in Table IV: the converged E_{xb} range between ≈ 150 and 250 meV. The use of mBSE for the E_{xb} estimation is justified by a direct comparison with the BSE prediction on a reduced

$11 \times 11 \times 11$ mesh. In general the BSE reference values are very well reproduced by the mBSE, with an error varying from 4% (SrZrO₃) to 8% (SrHfO₃). Our BSE-calculated E_{xb} for SrTiO₃ (205 meV) is consistent with previous BSE predictions of Begum *et al.* [16] (246 meV) and Sponza *et al.* [14] (220 meV). The difference with Begum’s result is due to the use of the SCAN functional in Ref. [16]. Increasing the k -point mesh up to $20 \times 20 \times 20$ within the mBSE leads to a lowering of E_{xb} to 165 meV. We note that the choice of the k -point mesh has a paramount effect on the final values; the change of E_{xb} between the $11 \times 11 \times 11$ and the well-converged $20 \times 20 \times 20$ mesh is between 0.056 eV (SrZrO₃) and 0.088 eV (KTaO₃); see Table IV.

2. Origin and character of main optical transitions

The octahedral crystal field that causes the splitting of the d states is the dominant factor for the formation of the observed two-structure spectra. In order to analyze the character of the transitions we display the JDOS in Fig. 5 (which provides a measure of the number of allowed optical transitions between initial and final states). Here and in the following the discussion of the optical transitions is given in terms of the band labeling shown in Fig. 6, where the conduction bands are denoted as c_n with $n = 1$ for the first conduction band and so on.

For KTaO₃ and SrTiO₃ the first structures (around peak p_1) are almost completely determined by transitions from the occupied oxygen manifold to the first three conduction bands (denoted as c_1 – c_3), i.e., $O-2p \rightarrow c_1$ – c_3 (the higher c_4 – c_9 conduction bands almost do not contribute to the first structures’ JDOS). For these two compounds the c_1 – c_3 manifolds have a main $TM-t_{2g}$ character, with a limited $O-p$ hybridization

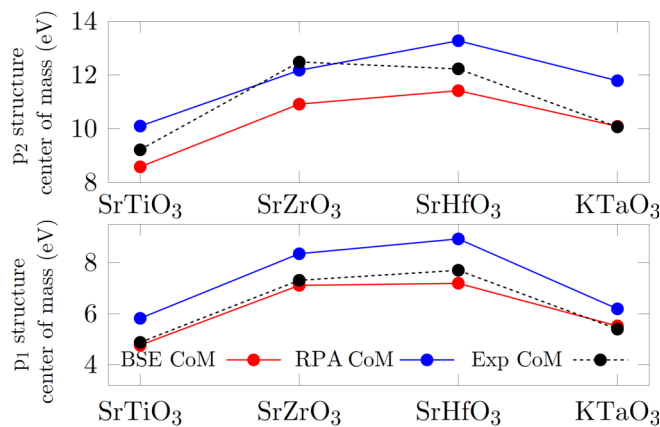


FIG. 4. Centers of mass (COMs) of the two main structures in the cubic compound spectra.

TABLE IV. Exciton binding energies E_{xb} in eV for the cubic materials, calculated through the BSE and mBSE approaches. The third row summarizes the percentage errors between the BSE reference values and the mBSE ones. The employed k -point meshes are specified in the second column ($20 \times 20 \times 20$ represents the converged mesh as described in Sec. II A). The calculated inverse static dielectric constants and screening length parameters λ (\AA^{-1}) used for the mBSE [Eq. (3)] are given.

	k mesh	SrTiO ₃	SrZrO ₃	SrHfO ₃	KTaO ₃
BSE	$11 \times 11 \times 11$	0.205	0.321	0.319	0.230
mBSE	$11 \times 11 \times 11$	0.195	0.308	0.293	0.215
% error		5	4	8	7
mBSE	$20 \times 20 \times 20$	0.149	0.275	0.258	0.160
ϵ_{∞}^{-1}		0.165	0.231	0.242	0.195
λ		1.463	1.457	1.448	1.420

away from the Γ point (between 5% and 15% for SrTiO₃ and between 2% and 23% for KTaO₃, as determined by G_0W_0 calculations on an $8 \times 8 \times 8$ k mesh).

The analysis of SrHfO₃ and SrZrO₃ optical transitions is complicated by the presence of band entanglement between the c_1 - c_3 manifold and the upper c_4 - c_9 manifold, not present in KTaO₃ and SrTiO₃ (where these two sets of bands are separated in energy; see Fig. 6). Similarly to SrTiO₃ and KTaO₃, the c_1 - c_3 bands possess a main TM- t_{2g} character, which however is not uniform in the Brillouin zone and exhibits a significant hybridization with O- p states (between 3% and 27% for SrZrO₃ and between 2% and 31% for SrZrO₃, as determined by G_0W_0 calculations on $8 \times 8 \times 8$ k meshes). Due to this band entanglement the JDOS shows some contributions to the p_1 structures from transitions to bands c_4 - c_9 (see Fig. 5). To ascertain the actual importance of these transitions and the relative significance of the c_1 - c_3 and c_4 - c_9 more quantitatively we list in Table V the BSE eigenvectors relative to the p_1 peak for each material in terms of the amplitude distribution (i.e., the total square amplitude) associated with transitions to bands c_1 - c_3 ($D_{c_1-c_3}^A = \sum_k \sum_{v \in O-2p} \sum_{c \in c_1-c_3} |A_{kvc}^A|^2$) and bands c_4 - c_9 ($D_{c_4-c_9}^A = \sum_k \sum_{v \in O-2p} \sum_{c \in c_4-c_9} |A_{kvc}^A|^2$). The eigenvalues listed in Table V are chosen as the transitions with the highest oscillator strength close to the p_1 peaks. Recalling that A_{kvc}^A is normalized ($\sum_{k,v,c} |A_{kvc}^A|^2 = 1$), the data in Table V indicate that transitions to c_1 - c_3 provide $\sim 90\%$ of the total spectral weight in SrZrO₃ and SrHfO₃, about 9% lower than the corresponding amplitudes in SrTiO₃ and KTaO₃.

Additional insights on the character of the dominant optical transitions can be extracted by the fat-band analysis of the BSE eigenvectors. This is displayed in Fig. 6 for the first nondark excitons as well as for A_{vck}^A with the highest oscillator

strength close to the p_1 peaks and p_2 peaks. As a general feature, common to all cubic materials, the contributions to $|A_{vck}^A|$ are predominantly localized at Γ (in particular for the first excitations, from the top of the valence band to the bottom of the conduction band) and, less intensively, along the Γ -X direction. The fat-band plots support the association of the p_1 peak with the transitions from the occupied O- p bands (blue) to t_{2g} (red, c_1 - c_3). These features hold not only for the A_{vck}^A related to the p_1 transitions, but more generally also for all bright eigenvectors in a ~ 0.3 eV range around these p_1 transitions.

B. La series

1. Comparison between BSE and RPA spectra

The optical conductivity spectra for the La-based perovskites are collected in Fig. 7. All members of the La series exhibit a qualitatively similar $\sigma(\omega)$ (with the exception of LaScO₃), characterized by two main different features: a low-intensity structure at low energies and a second peak at higher energies, broader and more intense. The low-intensity peak is mainly associated with a Mott-Hubbard type (MH) d - d fundamental gap, while the second is typically associated with a charge-transfer (CT) type gap [24,38,59]. LaCrO₃ in particular can be better described by a mixed MH/CT state, where the first peak is essentially merged with the CT transitions [38]. The band insulator LaScO₃ does not obviously show any Mott-like d - d transition.

The transition energies related to the first excitation are well reproduced already at the RPA level. The systematic redshifts produced by the excitonic effects [evaluated at $\sigma(\omega) \sim 0.3 \times 10^3 \Omega^{-1} \text{cm}^{-1}$] are reduced compared to the cubic compounds and vary from 0.3 eV (for LaTiO₃ and LaMnO₃) to

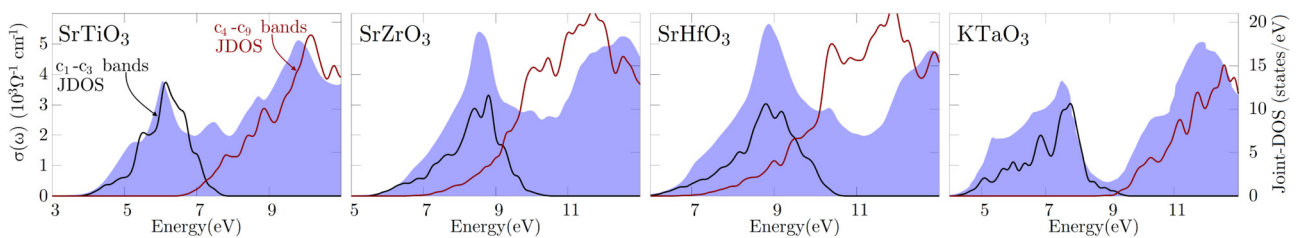


FIG. 5. Optical conductivity $\sigma(\omega)$ in the RPA (blue shaded background), along with the joint density of states associated with transitions to the first three conduction bands c_1 - c_3 (black lines) and to conduction bands c_4 - c_9 (red lines). All curves are obtained with an $11 \times 11 \times 11$ k -point mesh.

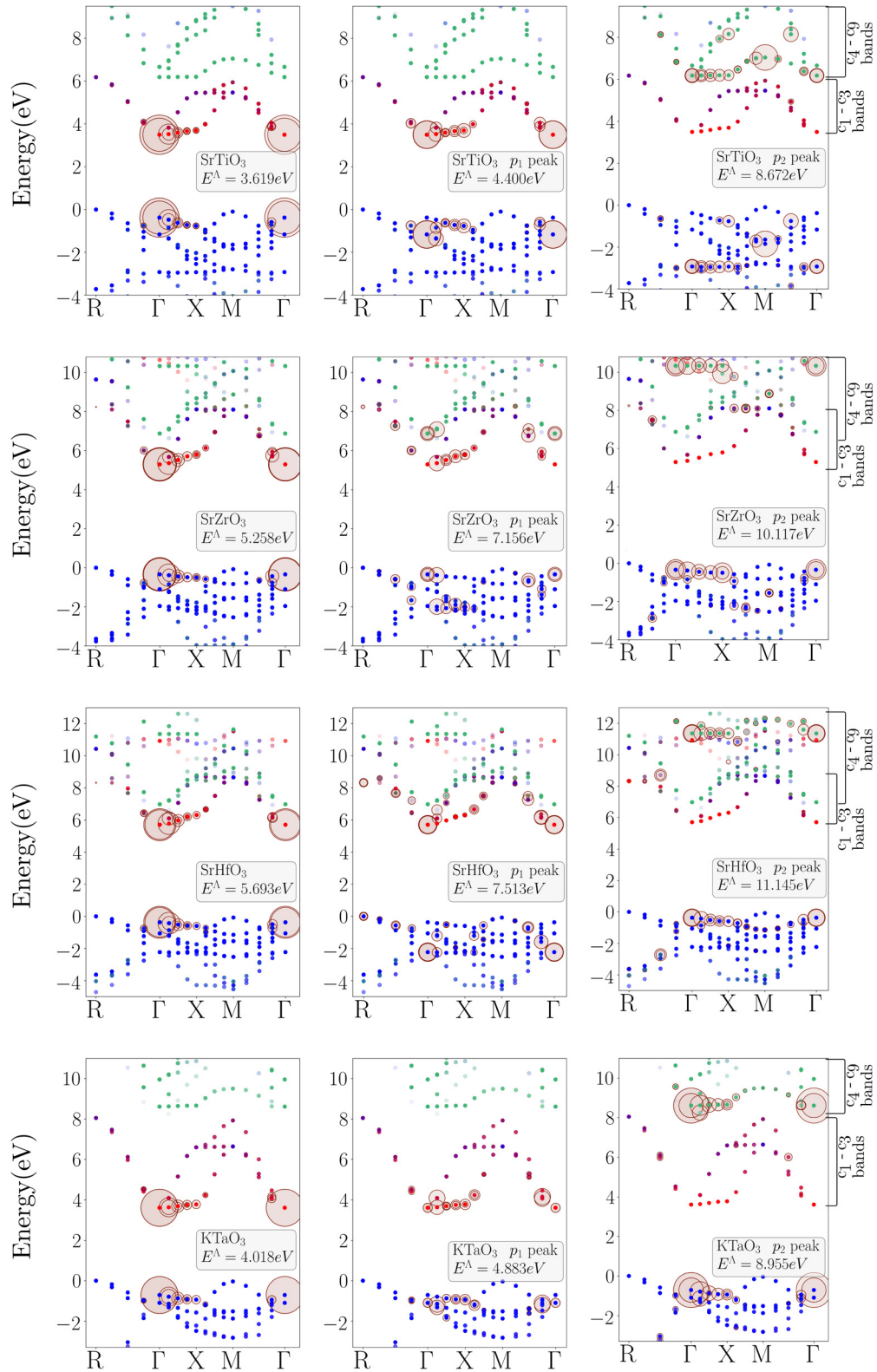


FIG. 6. Fat-band pictures for the cubic systems, obtained through G_0W_0 +BSE on an $8 \times 8 \times 8$ k -point grid. The circle radius corresponds to the contribution $|A_{kvc}^\lambda|^2$ to the e-h pair wave function at that k point. The left panels refer to the *first* nondark eigenvector of each material, the middle panels refer to the eigenvectors associated with the highest oscillator strengths close to the p_1 peaks, and the right panels to the eigenvectors with the highest oscillator strengths close to the p_2 peaks. The colors of the points in the band structures are associated with different orbital characters: blue for O p , red for TM t_{2g} , and green for TM e_g .

TABLE V. Comparison between BSE amplitude distributions D^Λ related respectively to the final states c_1-c_3 ($D_{c_1-c_3}^\Lambda = \sum_k \sum_{v \in O-2p} \sum_{c \in c_1-c_3} |A_{kvc}^\Lambda|^2$) and c_4-c_9 ($D_{c_4-c_9}^\Lambda = \sum_k \sum_{v \in O-2p} \sum_{c \in c_4-c_9} |A_{kvc}^\Lambda|^2$). E^Λ represent the corresponding BSE eigenvalues: the analyzed transitions are associated with the p_1 peaks. The data are obtained using an $11 \times 11 \times 11$ k -point mesh.

	SrTiO ₃	SrZrO ₃	SrHfO ₃	KTaO ₃
$D_{c_1-c_3}^\Lambda$	0.99	0.89	0.88	0.99
$D_{c_4-c_9}^\Lambda$	0.01	0.11	0.12	0.01
E^Λ (eV)	4.400	7.178	7.513	4.883

0.5 eV (LaCrO₃ and LaFeO₃) and 0.7 eV (LaVO₃). Therefore, when compared to the experimental curves, the BSE approach produces an underestimation of the first transition energies for almost all compounds. The only exception is LaTiO₃, where the optical gap is overestimated as a consequence of the corresponding overestimation of the experimental gap (0.1 eV) [59] obtained at the G_0W_0 level (≈ 0.5 eV, as described by the nonextrapolated case of [24]). The sources of the above deviations are discussed below for each compound. This involves both theoretical arguments and aspects of the experimental measurements (for instance, the available experimental data were obtained by different techniques at different temperatures, making a consistent comparison with computational data achieved at 0 K difficult; see Table S1 in the SM). The second structure, located at 7–8 eV, dominates the spectra and exhibits stronger excitonic effects, with redshifts [evaluated at $\sigma(\omega) \sim 3 \times 10^3 \Omega^{-1} \text{cm}^{-1}$] between 0.6 eV (LaCrO₃ and LaFeO₃) and 1.0 eV (LaVO₃). An improvement over the RPA is observed only for LaTiO₃, LaVO₃, and LaCrO₃; the quality of the agreement with the experimental curves is overall material dependent.

The ($p \rightarrow d$) band insulator LaScO₃ follows a trend dissimilar to the picture described above: it presents a single, wide, and intense peak with a rather strong excitonic red-

shift of 0.9 eV [evaluated at $\sigma(\omega) \sim 0.3 \times 10^3 \Omega^{-1} \text{cm}^{-1}$]. The disagreement between the measured and calculated spectrum should be traced back to the difference between the G_0W_0 and the experimental gap (≈ 1 eV [24]), which has been attributed to difficulties in measuring the long tail in the bottom part of the spectrum [24]. The exciton binding energies (listed in Table VI) fall within the 120 meV to 190 meV range and are overall smaller than their cubic nonmagnetic counterparts (with the exception of LaVO₃). The predicted higher E_{xb} for LaVO₃ is consistent with the larger experimental value of Lovinger *et al.* [61] (~ 0.6 eV). Recent experimental optical conductivity measurements [60] also highlight a splitting of the low-energy structure (visible as an additional shoulder at lower temperatures) which has been related to excitonic effects [61–63] and is correctly reproduced by the BSE data (but completely absent in the RPA curve). Compared to the full BSE, mBSE introduces an error ranging between 10% (LaScO₃) and 37% (LaVO₃), with a mean absolute error of 0.20 eV. The mBSE scheme therefore performs less satisfactorily for this subset than for the cubic nonmagnetic perovskites; LaVO₃ exhibits the larger discrepancy both in absolute and percentage values of the whole set, as shown in Fig. 8, where we collect the calculated (m)BSE excitonic binding energies, quasiparticle G_0W_0 gaps, and static dielectric constant for all materials included in the considered perovskites data set. To gain insight on the cause of the larger error observed for LaVO₃, we performed a mBSE calculation on top of the G_0W_0 band structure (while keeping the k mesh, μ , and λ fixed at the values of Table VI). In this manner the scissor operator is not required and we can isolate and gauge the effect of the model dielectric function approximation alone. The resulting mBSE@ G_0W_0 exciton binding energy is only slightly increased with respect to the mBSE value (0.299 eV vs 0.273 eV), and still much smaller than $E_{xb}^{BSE} = 0.434$ eV, implying that the disagreement mostly arises from the model dielectric function approximation. To verify this hypothesis we have conducted an additional BSE@ G_0W_0 calculation retaining only the

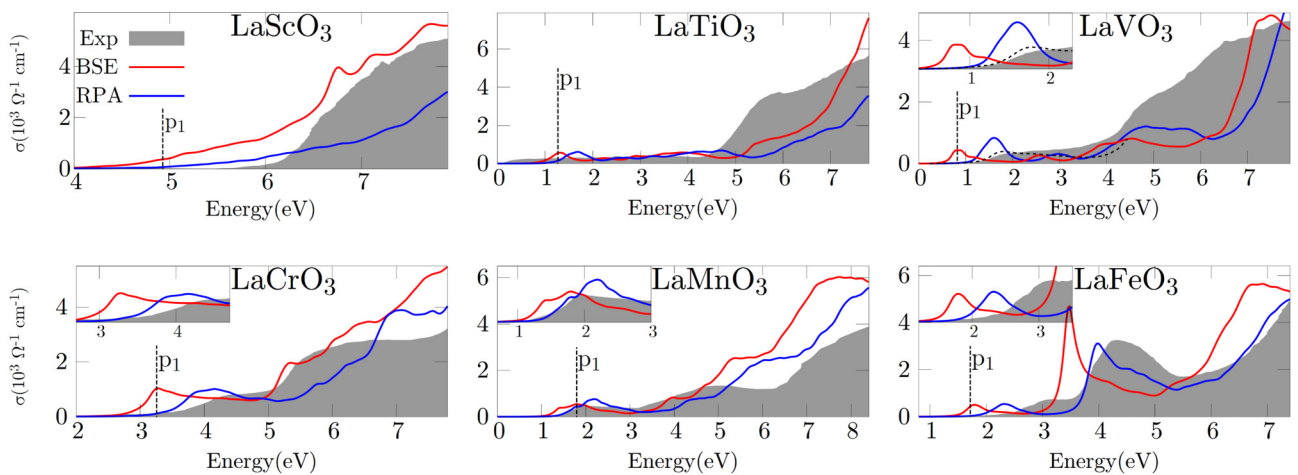


FIG. 7. $\sigma(\omega)$ within the RPA (blue line), BSE approach (red line), and experimental data (from Arima *et al.* [59]; the dashed line for LaVO₃ represents the optical conductivity measurement from Miyasaka *et al.* [60]). All curves are obtained through a $5 \times 5 \times 2|2 \times 2 \times 2$ k -averaging, except for LaScO₃, for which a $5 \times 5 \times 3|2 \times 2 \times 2$ mesh was used. The p_1 labels denote the first (low intensity) BSE structures.

TABLE VI. Exciton binding energies E_{xb} in eV for the La series compounds, calculated by mBSE and BSE approaches. Conventions used are the same as in Table IV.

	k -point mesh	LaTMO ₃					
		Sc	Ti	V	Cr	Mn	Fe
BSE	6 × 6 × 4	0.324	0.130	0.434	0.166	0.147	0.202
mBSE	6 × 6 × 4	0.292	0.145	0.273	0.200	0.181	0.162
% error		10	12	37	20	23	20
mBSE	10 × 10 × 6	0.189	0.134	0.263	0.171	0.160	0.116
ϵ_{∞}^{-1}		0.201	0.120	0.122	0.147	0.107	0.103
λ		1.462	1.349	1.420	1.393	1.335	1.336

diagonal elements of the screened exchange kernel. The resulting binding energy is $E_{xb}^{BSE\text{-diag only}} = 0.322$ eV, much closer to the mBSE@ G_0W_0 value of 0.299 eV than to E_{xb}^{BSE} with the full screened exchange kernel (0.434 eV). This proves that including off-diagonal elements in the inverse dielectric function and in the screened kernel is essential for accurately describing the excitonic properties of LaVO₃ and explains the limits of the model dielectric screening approximation for this material.

2. Origin and character of main optical transitions

Also for this series of compounds, we decode the character of the optical transition by analyzing the excitonic eigenvectors in a fat-band mode. Figure 9 presents the fat-band pictures related to the first nondark excitation and to the most intense oscillator strength of the p_1 peaks (as indicated in Sec. III B 1). The character of the excitonic wave function is closely connected to the electronic nature of the insulating state (band insulator, MH, CT, and mixed MH/CT) [38,59].

For the band-insulator LaScO₃ (top left) the direct transitions at Γ dominate the excitonic wave functions (only minor contributions can be seen along the Γ - X direction) which involve O- p to Sc- d excitations. The first (lowest) set of optical excitations for MH insulators LaTiO₃ (top right), LaVO₃ (middle left), and LaMnO₃ (bottom left) are determined by d - d transitions exclusively involving the two MH

subbands, whose states have a predominant TM- d character [25,38,64,65]. We note that contributions to eigenstates $A_{vc\mathbf{k}}^{\Delta}$ at Γ are almost negligible. This can be explained by recalling that $d \rightarrow d$ transitions are dipole forbidden at k points with a small point group equal to the full point group of the crystal, like the Γ point [66,67]. However, the remaining region of the BZ has a small point group with a lowered symmetry, thus allowing the $d \rightarrow d$ transitions determining the Mott peaks. The second main structures (for energies approximately larger than 4 eV) are instead determined by p - d transitions from the valence O- p bands (laying below the occupied MH subband) to the conduction MH subband; at higher energies transitions to La- d states are also involved (not shown).

For LaCrO₃ and LaFeO₃ optical experiments reported the coexistence of MH/CT-type excitations at the fundamental gap [59]. This was later confirmed by first-principles analyses which indicate a sizable admixture of O- p ($\approx 20\%$ and 30% for LaCrO₃ and LaFeO₃, respectively) and TM- d ($\approx 80\%$ and 70%) [24,25,38,68]. This mixed CT/MH nature of the optical excitations in LaFeO₃ is well captured by the BSE eigenvectors shown in the fat-band plots of Fig. 9. Moreover, the optical spectrum of LaFeO₃ exhibits a peculiar third intense peak at ~ 3 –4 eV, whose contributions are analyzed in Fig. 10. Transitions from the mixed O- p /Fe- d subband near the Fermi energy to the Fe- d states located at ~ 4 eV provide the majority of the total square amplitude ($\sum_{\mathbf{k}} \sum_{v \in \text{O-}p/\text{Fe-}d} \sum_{c \in \text{Fe-}d \sim 4 \text{ eV}} |A_{vc\mathbf{k}}^{\Delta}|^2 \sim 0.59$) and are particularly intense at the X and T points. A secondary contribution emerges from valence O- p states at ~ -2 eV to the conduction bands at ~ 2 eV (with a $\sim 30\%$ total square amplitude).

For LaCrO₃ the coexistence of MH/CT-type transitions at the optical gap is associated with an overlapping of the Mott and CT excitations in the spectrum [59] and has been explained in terms of a significant mixing of Cr- t_{2g} and O- p at the valence band top [25,38,68]. The optical conductivity in Fig. 7 only partially agrees with this picture: the energy separation between the p_1 peak and the CT structure is significantly overestimated and the optical gap possesses a dominant d - d character. This reduced mixed CT/MH character is due to a low O- p orbital character of the LaCrO₃ valence band maxima [24] (with an O- p percentage of 17%–20%). Considering the perturbative nature of the G_0W_0 scheme, this apparent discrepancy could originate from the PBE starting point. To test this hypothesis we performed an additional G_0W_0 +BSE calculation starting from hybrid functional orbitals (following the setup of Ref. [38], with an exchange fraction $\alpha = 0.15$). The results, shown in Fig. 11, lead to an improved agreement

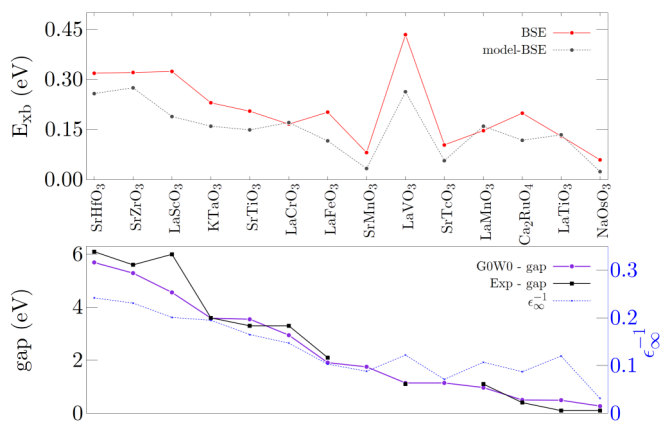


FIG. 8. Comparison between BSE and mBSE E_{xb} values calculated on the nonconverged k meshes (listed in Tables IV, VI, and VII). The lower graph displays the G_0W_0 and experimental gaps along with the inverse static dielectric constants.

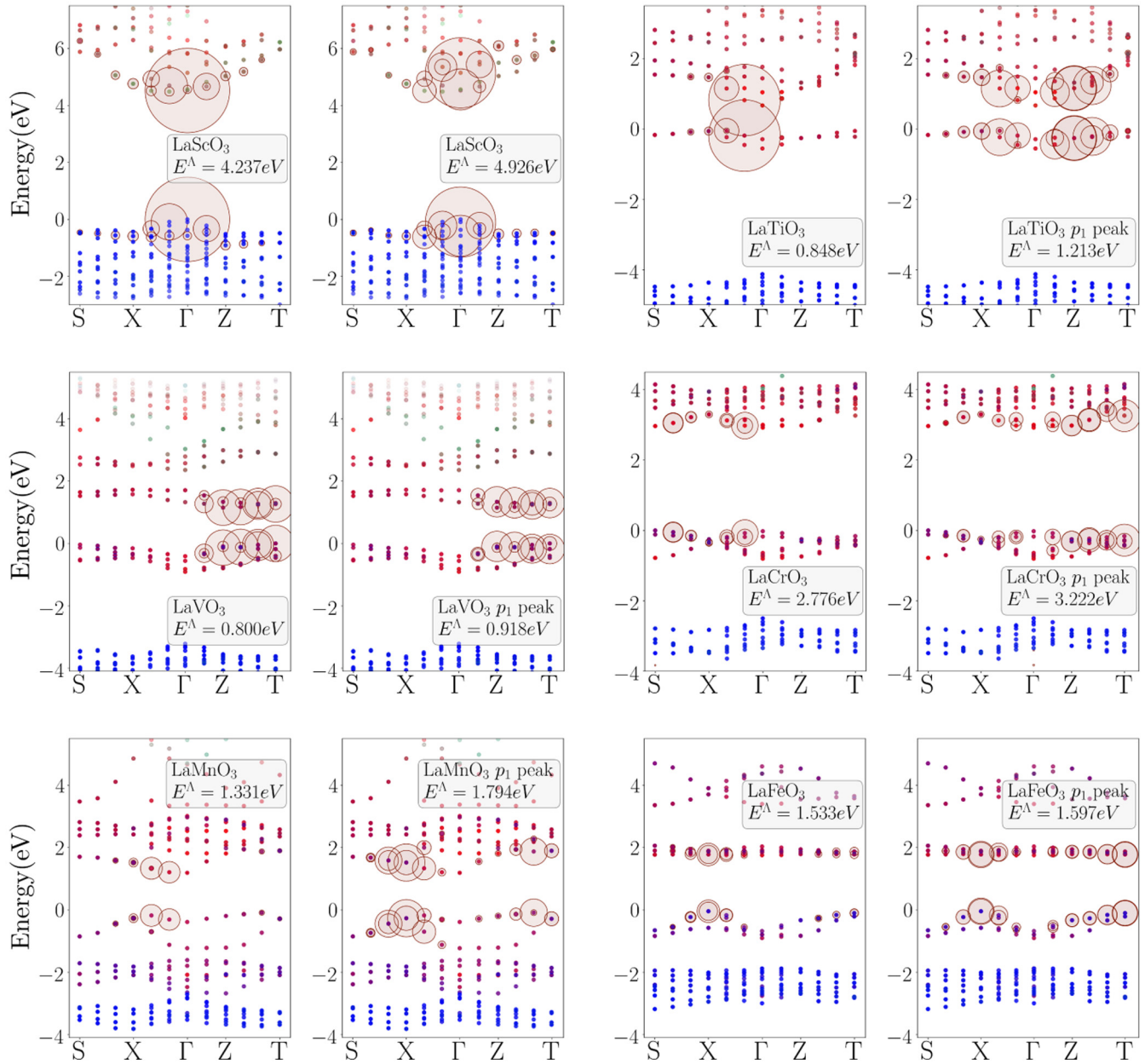


FIG. 9. Fat-band plots for members of the La series (LaTiO₃, LaVO₃, LaCrO₃, LaMnO₃, LaFeO₃, and LaScO₃). For each compound we show two panels: the left one refers to the *first* nondark eigenvector whereas the right one is related to the eigenvector with the highest oscillator strength close to the p_1 BSE structures (see Fig. 7). Color codings and labelings are similar to those adopted in Fig. 6: blue for O p , red for TM d , and green for La d .

with the experimental data. The oxygen character of the top of the valence band increases from $\sim 20\%$ to $\sim 30\%$, restoring the MH/CT mixed nature of the optical gap. The O- p valence bands below the MH subband are shifted toward higher energies, producing a reduction of the energy separation between the p_1 and CT peaks. However G_0W_0 on top of the Heyd-Scuseria-Ernzerhof (HSE) hybrid functional overestimates the experimental optical gap by ~ 0.6 eV (with BSE optical gap of 3.89 eV versus the experimental value of 3.30 eV [59]). Conversely, the calculations based on G_0W_0 @PBE (on the same k mesh) predict a smaller optical gap of 2.74 eV.

C. Ca₂RuO₄, NaOsO₃, and SrTMO₃ ($TM = Mn, Tc$)

1. Comparison between BSE and RPA spectra

We complete the discussion of the results by reporting the analysis of the optical transitions for the remaining compounds: Ca₂RuO₄, NaOsO₃, SrMnO₃, and SrTcO₃ [the computed $\sigma(\omega)$ are collected in Fig. 12]. For these compounds, a comparison with the measured optical conductivity is limited to NaOsO₃ [69] and Ca₂RuO₄ [70] (to the best of our knowledge, we are not aware of any experimental spectra for SrMnO₃ and SrTcO₃). For those materials only a qualitative agreement between theory and experiment is achieved.

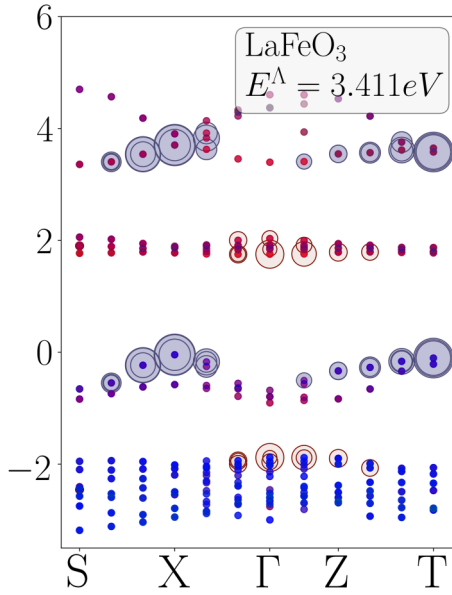


FIG. 10. Fat-band picture for A_{kvc} associated with the third peak of LaFeO_3 . The two main transition categories contributing to the eigenvector are distinguished by different colors.

The experimental spectrum of Ca_2RuO_4 exhibits three distinct peaks: 2 weak shoulders labeled α and β (following the nomenclature of Jung *et al.* [70]) and a third intense one at ~ 3 eV designated as γ . These peaks are correctly identified by

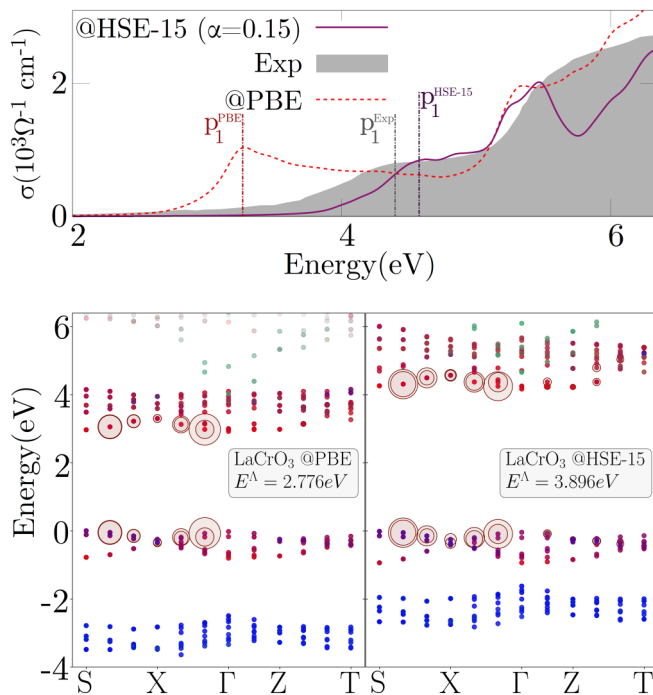


FIG. 11. Comparison between LaCrO_3 G_0W_0 +BSE spectra and fat-band pictures calculated from the PBE functional and from the hybrid functional (with an exchange fraction of 0.15). The p_1 peak of each spectrum is labeled. The fat-band pictures are associated with the first nondark transitions.

both RPA and BSE approaches, despite the lower intensities. $\sigma^{RPA}(\omega)$ underestimates the experimental onset, and the BSE slightly aggravates this discrepancy with a redshift of ~ 0.2 eV. The α and β peaks predicted by BSE exhibit a slightly more pronounced redshift (respectively ~ 0.3 eV and ~ 0.4 eV).

Despite retaining a transition metal of the same group, SrMnO_3 and SrTcO_3 exhibit rather different spectra. The 3d SrMnO_3 perovskite displays a wide and multip peaked structure between 2 eV and 4 eV. The excitonic corrections are prominent, with a significant enhancement of the peak at 2.8 eV associated with a redshift of ~ 0.6 eV (evaluated at $\sigma \sim 2 \times 10^3 \Omega^{-1} \text{cm}^{-1}$). For the 4d perovskite SrTcO_3 BSE does not substantially modify the peaks' intensity, but leads to a sizable redshift of about 0.4 eV for the first peak (evaluated at $\sigma \sim 2 \times 10^3 \Omega^{-1} \text{cm}^{-1}$). The 5d compound NaOsO_3 exhibits the highest ϵ_∞ within the data set (see Fig. 8 suggesting a strong electronic screening) and the lowest excitonic redshift among all considered systems (~ 0.1 eV; see Fig. 8). This is reminiscent of the BSE prediction for other 5d systems (e.g., iridates [12,15]), indicating relatively weak excitonic effects in extended 5d orbitals.

The calculated exciton binding energies, along with the parameters used for the constructing the model screening functions, are listed in Table VII. For this subset of materials, mBSE reproduces rather well the BSE binding energies E_{xb} .

2. Origin and character of main optical transitions

We discuss the nature of the main transitions based on the fat-band analysis shown in Fig. 13. Similarly to the previous cases, we focus our analysis on the first nondark excitations and on the main peaks in the first part of the optical spectra.

For SrTcO_3 both the optical gap and the sharp peak at 1.4 eV exhibit a clear Mott character. Although the greater contributions to the excitonic wave functions originate from the Z-T direction, the excitonic wave functions themselves are delocalized in the BZ and their amplitudes are suppressed at the Γ point, as expected from Mott-type $d-d$ transitions (see discussion for the La series). As already mentioned, SrMnO_3 displays marked differences: the uppermost valence bands exhibit a strong admixture of O- p and Mn- d (with a O- p percentage varying between 18% along the Γ -X direction and 46% along S-X) indicating an intermediate CT/MH nature of the optical gap [24]. The associated wave function is more localized than the one calculated for SrTcO_3 , with strong contributions only around the Γ -X direction.

The low-energy electronic structure of Ca_2RuO_4 has been widely studied and discussed [70–78]. The 4d electrons occupy the t_{2g} orbitals, with the e_g states well separated in energy and completely empty. Our G_0W_0 data, in agreement with previous computational studies [70,79], describe a t_{2g} manifold subjected to a further splitting, with the d_{xy} dominantly occupied and the d_{xz}/d_{yz} mixed and partially filled. The t_{2g} splitting has been associated with different mechanisms, including the rotation and tilting of the RuO_6 octahedra [72], spin-orbit interaction [73], c -axis contraction, and crystal field stabilization [74,75]. The O- p percentage varies between 14% and 25% for the highest valence band and between 20% and 24% for the lowest conduction band, indicating an admixture of p and d states with a predominantly MH $d-d$ optical gap

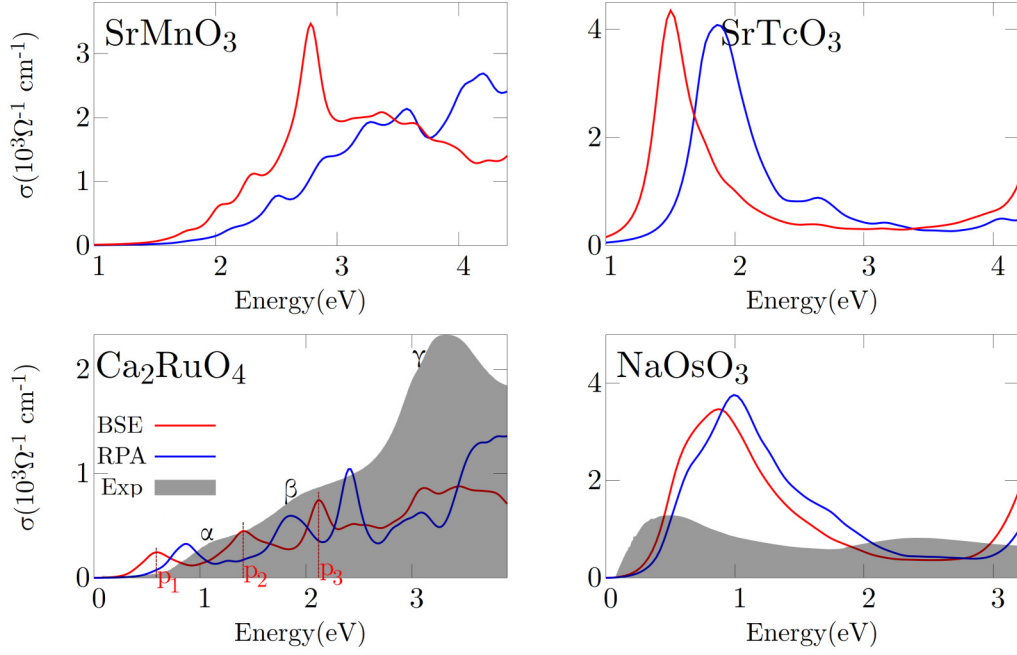


FIG. 12. $\sigma(\omega)$ within the RPA (blue line), BSE approach (red line), and experimental data; we could not find any experimental curve in literature for SrMnO₃ and SrTcO₃. α , β , and γ label Ca₂RuO₄ experimental curve's peaks, while p_1 , p_2 , and p_3 label the peaks of the BSE curve. SrMnO₃ and Ca₂RuO₄ curves are obtained through a $4 \times 4 \times 2 | 2 \times 2 \times 2$ k -averaging, SrTcO₃ through a $5 \times 5 \times 3 | 2 \times 2 \times 2$ one, and NaOsO₃ through $3 \times 3 \times 3 | 2 \times 2 \times 2$ one.

[24]. Our data suggest that the p_1 peak is determined by transitions between filled and empty t_{2g} bands, more specifically between filled d_{xy} states and conduction d_{xz}/d_{yz} states. The p_2 peak at ~ 1.5 eV can be assigned to transitions between the split d_{xz}/d_{yz} manifolds, whereas the p_3 peak at 2.2 eV is established by excitations from d_{xy} orbitals just below the Fermi energy to Ru- e_g states > 2 eV above the Fermi energy (see Fig. 14). The wide structure around 3 eV in the BSE spectrum is determined by excitations from the O- p bands near -3 eV under the Fermi energy toward the conduction d_{xz}/d_{yz} orbitals.

IV. SUMMARY AND CONCLUSIONS

We have performed a systematic investigation of the optical properties of a selected set of transition metal oxide perovskites by *ab initio* G_0W_0 +BSE. The 14 compounds were selected to constitute a minimal data set, representative of

the variety of structural and electronic properties characteristic of this class of perovskites. The solution of the BSE equation proves to be decisive to obtain a quantitative agreement between the theoretical and experimental spectra for the cubic perovskites SrTiO₃, SrHfO₃, SrZrO₃, and KTaO₃. A pronounced spectral weight transfer is visible in their optical conductivity line shapes (with an average redshift at the onset of 1.03 eV) and can be related to prominent excitonic contributions. This confirms and extends the previous studies on SrTiO₃. To investigate the origin of the main structures of the spectra we analyzed the e-h coupling coefficients associated with the most intense oscillator strengths. The contributions from transitions toward different conduction band manifolds are examined, and the role of band overlapping in SrZrO₃ and SrHfO₃ is discussed.

Comparisons with the reference experimental data have been discussed for the La series, NaOsO₃, and Ca₂RuO₄. The main structures visible in the experimental spectra are

TABLE VII. Exciton binding energies E_{xb} in eV for Ca₂RuO₄, NaOsO₃, and $STMO_3$ ($TM = Mn, Tc$), calculated through the mBSE and BSE approaches. Conventions used are the same as in Table IV.

	k mesh	SrMnO ₃	SrTcO ₃	Ca ₂ RuO ₄	NaOsO ₃
BSE	$4 \times 4 \times 2$			0.199	
	$5 \times 5 \times 3$	0.081	0.104		0.059
mBSE	$4 \times 4 \times 2$			0.165	
	$5 \times 5 \times 3$	0.077	0.106		0.051
% error		5	2	17	14
mBSE	$8 \times 8 \times 4$	0.034		0.118	
	$9 \times 9 \times 6$		0.057		0.024
ϵ_∞^{-1}		0.088	0.071	0.087	0.031
λ		1.340	1.329	1.225	1.109

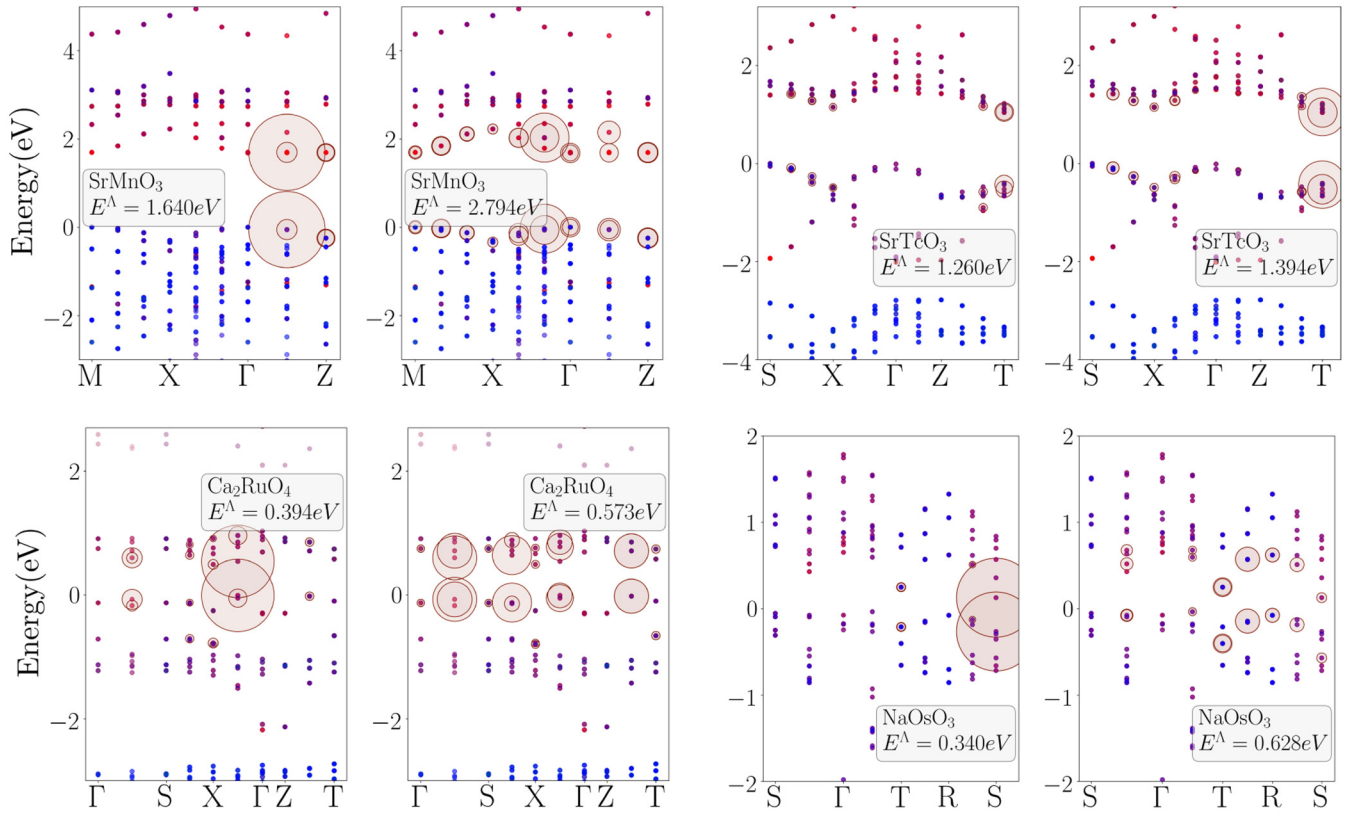


FIG. 13. Fat-band pictures for SrMnO_3 , SrTcO_3 , Ca_2RuO_4 , and NaOsO_3 . The left column refers to the *first* nondark eigenvector of each material, the right column to the eigenvectors associated with the highest peaks in the first structures. Color codings and labelings are analogous to those adopted in Fig. 9: blue for O p , red for TM t_{2g} , and green for Sr/Ca/Na d .

correctly identified in both RPA and BSE approaches with similar line shapes. The excitonic corrections for this subset can be summarized as a redshift of the entire spectra, with an average value of 0.5 eV and reduced peak enhancements (with LaFeO_3 as partial exception). The BSE approach, however, consistently underestimates the experimental onset by 0.3–1.0 eV and incorrectly describes the mixed MH/CT nature of LaCrO_3 's optical gap. Additional calculations based on hybrid functionals displayed significant improvements with respect to the overall optical conductivity line shape, optical band gap value, and character. Hence employing hybrid functionals as a starting point may represent a promising route for further investigations. The exciton binding energies were

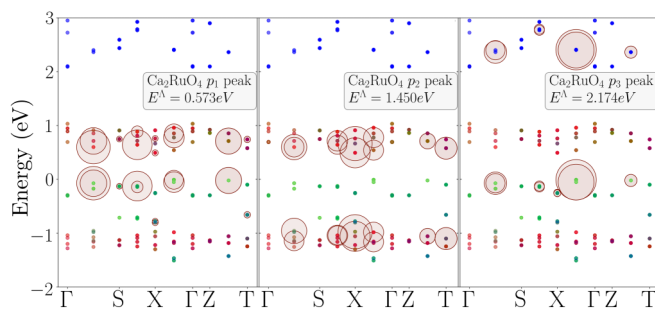


FIG. 14. Fat-band picture for $A_{\mathbf{k}vib}$ related to the first three BSE peaks of Ca_2RuO_4 . Green color for Ru $d_{x^2-y^2}$, red for mixed Ru d_{xz}/d_{yz} , blue for Ru e_g .

calculated through a mBSE approach. This method introduces two approximations: a scissor operator to mimic the quasiparticle shifts and a model dielectric function to determine the dielectric screening. The lower computational cost allows us to achieve converged E_{xb} with respect to the k -point mesh. To assess the validity of this approach, we benchmarked the mBSE-calculated E_{xb} against the G_0W_0 +BSE values obtained with the same k -point mesh. The BSE values are very well reproduced for the cubic subset [with a mean absolute percentage error (MAPE) of 6%] and for SrMnO_3 , SrTcO_3 , Ca_2RuO_4 , and NaOsO_3 (with a MAPE of 9%). The discrepancies for the La series are larger, with a MAPE of 20%; the largest outlier is LaVO_3 , primarily due to the diagonal dielectric screening approximation.

The overall agreement with experimental data is satisfactory, also considering the technical difficulties that hamper a precise measurement of optical spectra for TMO perovskites, and the tendency of this class of materials to be subjected to chemical defect (e.g., oxygen vacancies or presence of TM impurities). Our reported data represent a comprehensive map of the optical and excitonic properties of complex TMO and should serve as a reference for future calculations and experiments.

ACKNOWLEDGMENTS

The computational results presented have been achieved using the Vienna Scientific Cluster (VSC) and the CINECA

HPC infrastructure. Z.E.Y and C.F. acknowledge financial support from FWF (Austrian Science Fund) and Indian De-

partment of Science and Technology (DST) project INDOX (Project No. I1490-N19).

-
- [1] R. von Helmolt, J. Wecker, B. Holzapfel, L. Schultz, and K. Samwer, Giant Negative Magnetoresistance in Perovskite-Like $\text{La}_{2/3}\text{Ba}_{1/3}\text{MnO}_x$ Ferromagnetic Films, *Phys. Rev. Lett.* **71**, 2331 (1993).
- [2] M. B. Salamon and M. Jaime, The physics of manganites: Structure and transport, *Rev. Mod. Phys.* **73**, 583 (2001).
- [3] K. Wang, J.-M. Liu, and Z. Ren, Multiferroicity: The coupling between magnetic and polarization orders, *Adv. Phys.* **58**, 321 (2009).
- [4] M. Imada, A. Fujimori, and Y. Tokura, Metal-insulator transitions, *Rev. Mod. Phys.* **70**, 1039 (1998).
- [5] J. G. Bednorz and K. A. Müller, Possible high- T_c superconductivity in the Ba-La-Cu-O system, *Z. Phys. B* **64**, 189 (1986).
- [6] Y. Tokura, Correlated-electron physics in transition-metal oxides, *Phys. Today* **56(7)**, 50 (2003).
- [7] A. Ohtomo and H. Y. Hwang, A high-mobility electron gas at the $\text{LaAlO}_3/\text{SrTiO}_3$ heterointerface, *Nature (London)* **427**, 423 (2004).
- [8] C. N. R. Rao, Charge, spin, and orbital ordering in the perovskite manganates, $\text{Ln}_{1-x}\text{A}_x\text{MnO}_3$ (Ln = rare earth, A = Ca or Sr), *J. Phys. Chem. B* **104**, 5877 (2000).
- [9] W. Witczak-Krempa, G. Chen, Y. B. Kim, and L. Balents, Correlated quantum phenomena in the strong spin-orbit regime, *Annu. Rev. Condens. Matter Phys.* **5**, 57 (2014).
- [10] C. Martins, M. Aichhorn, and S. Biermann, Coulomb correlations in $4d$ and $5d$ oxides from first principles—or, how spin-orbit materials choose their effective orbital degeneracies, *J. Phys.: Condens. Matter* **29**, 263001 (2017).
- [11] P. Liu, J. He, B. Kim, S. Khmelevskiy, A. Toschi, G. Kresse, and C. Franchini, Comparative *ab initio* study of the structural, electronic, magnetic, and dynamical properties of LiOsO_3 and NaOsO_3 , *Phys. Rev. Mater.* **4**, 045001 (2020).
- [12] P. Liu and C. Franchini, Advanced first-principle modeling of relativistic Ruddlesden-Popper strontium iridates, *Appl. Sci.* **11**, 2527 (2021).
- [13] J. He and C. Franchini, Structural determination and electronic properties of the $4d$ perovskite SrPdO_3 , *Phys. Rev. B* **89**, 045104 (2014).
- [14] L. Sponza, V. Véniard, F. Sottile, C. Giorgetti, and L. Reining, Role of localized electrons in electron-hole interaction: The case of SrTiO_3 , *Phys. Rev. B* **87**, 235102 (2013).
- [15] P. Liu, B. Kim, X.-Q. Chen, D. D. Sarma, G. Kresse, and C. Franchini, Relativistic $\text{GW}+\text{BSE}$ study of the optical properties of Ruddlesden-Popper iridates, *Phys. Rev. Mater.* **2**, 075003 (2018).
- [16] V. Begum, M. E. Gruner, and R. Pentcheva, Role of the exchange-correlation functional on the structural, electronic, and optical properties of cubic and tetragonal SrTiO_3 including many-body effects, *Phys. Rev. Mater.* **3**, 065004 (2019).
- [17] C. Lane and J.-X. Zhu, Landscape of coexisting excitonic states in the insulating single-layer cuprates and nickelates, *Phys. Rev. B* **101**, 155135 (2020).
- [18] G. Onida, L. Reining, and A. Rubio, Electronic excitations: Density-functional versus many-body Green's-function approaches, *Rev. Mod. Phys.* **74**, 601 (2002).
- [19] S. Albrecht, L. Reining, R. Del Sole, and G. Onida, *Ab Initio* Calculation of Excitonic Effects in the Optical Spectra of Semiconductors, *Phys. Rev. Lett.* **80**, 4510 (1998).
- [20] M. van Schilfgaarde, T. Kotani, and S. Faleev, Quasiparticle Self-Consistent GW Theory, *Phys. Rev. Lett.* **96**, 226402 (2006).
- [21] L. Hedin, New method for calculating the one-particle Green's function with application to the electron-gas problem, *Phys. Rev.* **139**, A796 (1965).
- [22] G. Strinati, H. J. Mattausch, and W. Hanke, Dynamical aspects of correlation corrections in a covalent crystal, *Phys. Rev. B* **25**, 2867 (1982).
- [23] M. S. Hybertsen and S. G. Louie, First-Principles Theory of Quasiparticles: Calculation of Band Gaps in Semiconductors and Insulators, *Phys. Rev. Lett.* **55**, 1418 (1985).
- [24] Z. Ergönenc, B. Kim, P. Liu, G. Kresse, and C. Franchini, Converged GW quasiparticle energies for transition metal oxide perovskites, *Phys. Rev. Mater.* **2**, 024601 (2018).
- [25] Y. Nohara, S. Yamamoto, and T. Fujiwara, Electronic structure of perovskite-type transition metal oxides LaMO_3 ($M = \text{Ti} \sim \text{Cu}$) by $U + \text{GW}$ approximation, *Phys. Rev. B* **79**, 195110 (2009).
- [26] S. Lany, Band-structure calculations for the $3d$ transition metal oxides in GW , *Phys. Rev. B* **87**, 085112 (2013).
- [27] C. Franchini, R. Kováčik, M. Marsman, S. S. Murthy, J. He, C. Ederer, and G. Kresse, Maximally localized Wannier functions in LaMnO_3 within $\text{PBE}+U$, hybrid functionals, and partially self-consistent GW : An efficient route to construct *ab initio* tight-binding parameters for e_g perovskites, *J. Phys.: Condens. Matter* **24**, 235602 (2012).
- [28] S. Ryee, S. W. Jang, H. Kino, T. Kotani, and M. J. Han, Quasiparticle self-consistent GW calculation of Sr_2RuO_4 and SrRuO_3 , *Phys. Rev. B* **93**, 075125 (2016).
- [29] L. X. Benedict and E. L. Shirley, *Ab initio* calculation of $\epsilon_2(\omega)$ including the electron-hole interaction: Application to GaN and CaF_2 , *Phys. Rev. B* **59**, 5441 (1999).
- [30] S. Albrecht, L. Reining, G. Onida, V. Olevano, and R. Del Sole, Albrecht *et al.*, Reply, *Phys. Rev. Lett.* **83**, 3971 (1999).
- [31] R. Laskowski, N. E. Christensen, G. Santi, and C. Ambrosch-Draxl, *Ab initio* calculations of excitons in GaN , *Phys. Rev. B* **72**, 035204 (2005).
- [32] I. Aguilera, J. Vidal, P. Wahnón, L. Reining, and S. Botti, First-principles study of the band structure and optical absorption of CuGaS_2 , *Phys. Rev. B* **84**, 085145 (2011).
- [33] F. Fuchs, C. Rödl, A. Schleife, and F. Bechstedt, Efficient $\mathcal{O}(N^2)$ approach to solve the Bethe-Salpeter equation for excitonic bound states, *Phys. Rev. B* **78**, 085103 (2008).
- [34] M. Bokdam, T. Sander, A. Stroppa, S. Picozzi, D. D. Sarma, C. Franchini, and G. Kresse, Role of polar phonons in the photoexcited state of metal halide perovskites, *Sci. Rep.* **6**, 28618 (2016).
- [35] D. Kammerlander, S. Botti, M. A. L. Marques, A. Marini, and C. Attaccalite, Speeding up the solution of the Bethe-Salpeter

- equation by a double-grid method and Wannier interpolation, *Phys. Rev. B* **86**, 125203 (2012).
- [36] M. Rohlfing and S. G. Louie, Electron-hole excitations and optical spectra from first principles, *Phys. Rev. B* **62**, 4927 (2000).
- [37] D. Rocca, Y. Ping, R. Gebauer, and G. Galli, Solution of the Bethe-Salpeter equation without empty electronic states: Application to the absorption spectra of bulk systems, *Phys. Rev. B* **85**, 045116 (2012).
- [38] J. He and C. Franchini, Screened hybrid functional applied to $3d^0 \rightarrow 3d^8$ transition-metal perovskites LaMO_3 ($M = \text{Sc-Cu}$): Influence of the exchange mixing parameter on the structural, electronic, and magnetic properties, *Phys. Rev. B* **86**, 235117 (2012).
- [39] See Supplemental Material at <http://link.aps.org/supplemental/10.1103/PhysRevMaterials.5.074601> for a summary of the setup specifications for the experimental spectra, a comparison between $\sigma(\omega)$ with different averaging configurations for SrTiO_3 , and the atomic positions used.
- [40] G. Kresse and J. Hafner, *Ab initio* molecular dynamics for liquid metals, *Phys. Rev. B* **47**, 558 (1993).
- [41] G. Kresse and J. Furthmüller, Efficient iterative schemes for *ab initio* total-energy calculations using a plane-wave basis set, *Phys. Rev. B* **54**, 11169 (1996).
- [42] P. E. Blöchl, Projector augmented-wave method, *Phys. Rev. B* **50**, 17953 (1994).
- [43] J. P. Perdew, K. Burke, and M. Ernzerhof, Generalized Gradient Approximation Made Simple, *Phys. Rev. Lett.* **77**, 3865 (1996).
- [44] S. L. Dudarev, G. A. Botton, S. Y. Savrasov, C. J. Humphreys, and A. P. Sutton, Electron-energy-loss spectra and the structural stability of nickel oxide: An LSDA+ U study, *Phys. Rev. B* **57**, 1505 (1998).
- [45] S. Steiner, S. Khmelevskiy, M. Marsmann, and G. Kresse, Calculation of the magnetic anisotropy with projected-augmented-wave methodology and the case study of disordered $\text{Fe}_{1-x}\text{Co}_x$ alloys, *Phys. Rev. B* **93**, 224425 (2016).
- [46] M. Shishkin and G. Kresse, Implementation and performance of the frequency-dependent GW method within the PAW framework, *Phys. Rev. B* **74**, 035101 (2006).
- [47] R. Del Sole, L. Reining, and R. W. Godby, GW approximation for electron self-energies in semiconductors and insulators, *Phys. Rev. B* **49**, 8024 (1994).
- [48] M. Gajdoš, K. Hummer, G. Kresse, J. Furthmüller, and F. Bechstedt, Linear optical properties in the projector-augmented wave methodology, *Phys. Rev. B* **73**, 045112 (2006).
- [49] M. Rohlfing and S. G. Louie, Electron-Hole Excitations in Semiconductors and Insulators, *Phys. Rev. Lett.* **81**, 2312 (1998).
- [50] T. Sander, E. Maggio, and G. Kresse, Beyond the Tamm-Dancoff approximation for extended systems using exact diagonalization, *Phys. Rev. B* **92**, 045209 (2015).
- [51] S. M. Dancoff, Non-adiabatic meson theory of nuclear forces, *Phys. Rev.* **78**, 382 (1950).
- [52] P. H. Hahn, K. Seino, W. G. Schmidt, J. Furthmüller, and F. Bechstedt, Quasiparticle and excitonic effects in the optical spectra of diamond, SiC, Si, GaP, GaAs, InP, and AlN, *Phys. Status Solidi B* **242**, 2720 (2005).
- [53] L. Adamska and P. Umari, Bethe-Salpeter equation approach with electron-phonon coupling for exciton binding energies, *Phys. Rev. B* **103**, 075201 (2021).
- [54] A. Tal, P. Liu, G. Kresse, and A. Pasquarello, Accurate optical spectra through time-dependent density functional theory based on screening-dependent hybrid functionals, *Phys. Rev. Res.* **2**, 032019(R) (2020).
- [55] Z. Muhammad, P. Liu, R. Ahmad, S. Jalali Asadabadi, C. Franchini, and I. Ahmad, Tunable relativistic quasiparticle electronic and excitonic behavior of the $\text{FAPb}(\text{I}_{1-x}\text{Br}_x)_3$ alloy, *Phys. Chem. Chem. Phys.* **22**, 11943 (2020).
- [56] P. Liu, C. Franchini, M. Marsman, and G. Kresse, Assessing model-dielectric-dependent hybrid functionals on the antiferromagnetic transition-metal monoxides MnO, FeO, CoO, and NiO, *J. Phys.: Condens. Matter* **32**, 015502 (2019).
- [57] F. Sottile, Response functions of semiconductors and insulators: From the Bethe-Salpeter equation to time-dependent density functional theory, Ph.D. thesis, École Polytechnique X, 2003.
- [58] A. Molina-Sánchez, D. Sangalli, K. Hummer, A. Marini, and L. Wirtz, Effect of spin-orbit interaction on the optical spectra of single-layer, double-layer, and bulk MoS_2 , *Phys. Rev. B* **88**, 045412 (2013).
- [59] T. Arima, Y. Tokura, and J. B. Torrance, Variation of optical gaps in perovskite-type $3d$ transition-metal oxides, *Phys. Rev. B* **48**, 17006 (1993).
- [60] S. Miyasaka, Y. Okimoto, and Y. Tokura, Anisotropy of Mott-Hubbard gap transitions due to spin and orbital ordering in LaVO_3 and YVO_3 , *J. Phys. Soc. Jpn.* **71**, 2086 (2002).
- [61] D. J. Lovinger, M. Brahlek, P. Kissin, D. M. Kennes, A. J. Millis, R. Engel-Herbert, and R. D. Averitt, Influence of spin and orbital fluctuations on Mott-Hubbard exciton dynamics in LaVO_3 thin films, *Phys. Rev. B* **102**, 115143 (2020).
- [62] M. Kim, Signatures of spin-orbital states of t_{2g}^2 system in optical conductivity: RVO_3 ($R = \text{Y}$ and La), *Phys. Rev. B* **97**, 155141 (2018).
- [63] J. Reul, A. A. Nugroho, T. T. M. Palstra, and M. Grüninger, Probing orbital fluctuations in RVO_3 ($R = \text{Y}$, Gd , or Ce) by ellipsometry, *Phys. Rev. B* **86**, 125128 (2012).
- [64] J. Varignon, M. Bibes, and A. Zunger, Origin of band gaps in $3d$ perovskite oxides, *Nat. Commun.* **10**, 1658 (2019).
- [65] B. Kim, P. Liu, J. M. Tomczak, and C. Franchini, Strain-induced tuning of the electronic Coulomb interaction in $3d$ transition metal oxide perovskites, *Phys. Rev. B* **98**, 075130 (2018).
- [66] C. Rödl and F. Bechstedt, Optical and energy-loss spectra of the antiferromagnetic transition metal oxides MnO, FeO, CoO, and NiO including quasiparticle and excitonic effects, *Phys. Rev. B* **86**, 235122 (2012).
- [67] B. Friedhelm, *Many-Body Approach to Electronic Excitations: Concepts and Applications*, Springer Series in Solid-State Sciences (Springer, Berlin, 2016).
- [68] Z. Yang, Z. Huang, L. Ye, and X. Xie, Influence of parameters U and J in the LSDA+ U method on electronic structure of the perovskites LaMO_3 ($M = \text{Cr}$, Mn , Fe , Co , Ni), *Phys. Rev. B* **60**, 15674 (1999).
- [69] I. L. Vecchio, A. Perucchi, P. Di Pietro, O. Limaj, U. Schade, Y. Sun, M. Arai, K. Yamaura, and S. Lupi, Infrared evidence of a slater metal-insulator transition in NaOsO_3 , *Sci. Rep.* **3**, 2990 (2013).

- [70] J. H. Jung, Z. Fang, J. P. He, Y. Kaneko, Y. Okimoto, and Y. Tokura, Change of Electronic Structure in Ca_2RuO_4 Induced by Orbital Ordering, *Phys. Rev. Lett.* **91**, 056403 (2003).
- [71] D. Sutter, C. G. Fatuzzo, S. Moser, M. Kim, R. Fittipaldi, A. Vecchione, V. Granata, Y. Sassa, F. Cossalter, G. Gatti, M. Grioni, H. M. Rønnow, N. C. Plumb, C. E. Matt, M. Shi, M. Hoesch, T. K. Kim, T.-R. Chang, H.-T. Jeng, C. Jozwiak *et al.*, Hallmarks of Hund's coupling in the Mott insulator Ca_2RuO_4 , *Nat. Commun.* **8**, 15176 (2017).
- [72] T. Mizokawa, L. H. Tjeng, G. A. Sawatzky, G. Ghiringhelli, O. Tjernberg, N. B. Brookes, H. Fukazawa, S. Nakatsuji, and Y. Maeno, Spin-Orbit Coupling in the Mott Insulator Ca_2RuO_4 , *Phys. Rev. Lett.* **87**, 077202 (2001).
- [73] C. G. Fatuzzo, M. Dantz, S. Fatale, P. Olalde-Velasco, N. E. Shaik, B. Dalla Piazza, S. Toth, J. Pellicciari, R. Fittipaldi, A. Vecchione, N. Kikugawa, J. S. Brooks, H. M. Rønnow, M. Grioni, C. Rüegg, T. Schmitt, and J. Chang, Spin-orbit-induced orbital excitations in Sr_2RuO_4 and Ca_2RuO_4 : A resonant inelastic x-ray scattering study, *Phys. Rev. B* **91**, 155104 (2015).
- [74] E. Gorelov, M. Karolak, T. O. Wehling, F. Lechermann, A. I. Lichtenstein, and E. Pavarini, Nature of the Mott Transition in Ca_2RuO_4 , *Phys. Rev. Lett.* **104**, 226401 (2010).
- [75] G. Zhang and E. Pavarini, Mott transition, spin-orbit effects, and magnetism in Ca_2RuO_4 , *Phys. Rev. B* **95**, 075145 (2017).
- [76] G. Zhang and E. Pavarini, Higgs mode and stability of xy -orbital ordering in Ca_2RuO_4 , *Phys. Rev. B* **101**, 205128 (2020).
- [77] G.-Q. Liu, Competition between spin-orbit coupling and magnetic exchange splitting in Ca_2RuO_4 , *Phys. Rev. B* **88**, 104428 (2013).
- [78] T. Hotta and E. Dagotto, Prediction of Orbital Ordering in Single-Layered Ruthenates, *Phys. Rev. Lett.* **88**, 017201 (2001).
- [79] Z. Fang, N. Nagaosa, and K. Terakura, Orbital-dependent phase control in $\text{Ca}_{2-x}\text{Sr}_x\text{RuO}_4$ ($0 \leq x \leq 0.5$), *Phys. Rev. B* **69**, 045116 (2004).